4 The Handling and Transporting of Polymer Particulate Solids

In this chapter we deal with the entire ''journey'' of polymeric particulate solids, from the polymerization reactor to the shaped and structured finished product. The reader is referred to Chapter 1, which discusses all the processes and elementary steps involved in this journey.

The products of polymerization reactors are most often in particulate form: gas phase and slurry reactors produce porous spherical particulates about $300\,\mu m$ in diameter; emulsion reactors produce ultrafine $0.1\,\mu m$-diameter powder particulates; and suspension reactors produce beads that are $100–1000\,\mu m$ in diameter. Except for the gas-phase reactor, the particulate product stream has to be dried. The particulate reactor products are then transported in finished form to storage silos. Since they do not contain the necessary ''stabilizer package,'' and since, fine particulates are in general, more difficult to feed in compounding and final fabrication processing equipment, the following steps are taken. The particulates are transported in fluidized form to conical blenders, where stabilizing additives are spray-mixed onto them. From there, they are metered by weight-in-loss feeders with feed screws into large, twin-rotor melting extruders where melting and intimate mixing of the stabilizers are accomplished. Large, multihole, generally underwater strand dies with fast rotating knife blades in contact with the die-hole ring produce pellets of typical cylindrical dimension, that is, 0.3 cm diameter and 0.3 cm height. The molten pellets are cooled skin-deep by water in turbulent flow in the water box and transported as slurry for further cooling, spin-drying, storage, and shipping into 50-lb bags, 1000 lb gaylords or railroad cars. Typical polymer particulates are shown in Fig. 4.1.

As we pointed out in Chapter 1, the preceding describes the postreactor ''finishing'' operation. The pellets are then shipped to be compounded, namely, blended with fillers, colorants, or other polymers, where after melting, mixing, and reacting, they form physical
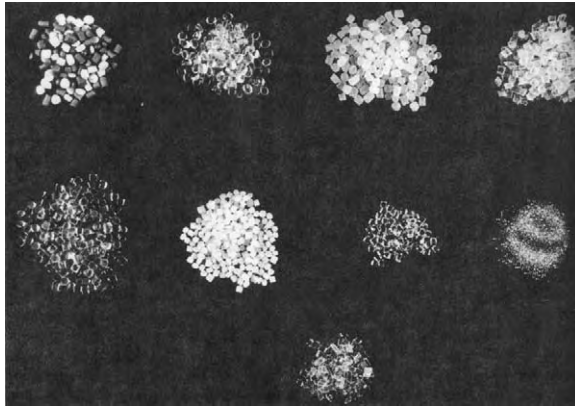
Fig. 4.1   Typical polymer particulates.

or reactive blends, as we shall see in Chapter 11. The pellets are meter-fed into twin rotor compounding equipment and exit again out of multihole dies to be pelletized as hot strands or underwater; in both cases, they are water-cooled and dried, packaged, and shipped to final polymer product fabricators. Finally, pellets are fed into single-rotor shaping processing equipment, such as single screw extruders or injection molding machines. For water-absorbing polymers, such as PET and polyamide (PA), the pellets are dried by hot air for 2 to 4 hours before processing, and transported in airtight conduits in fluidized form, to hoppers sealed from the atmosphere.

All the preceding "particulate handling steps" are affected by the unique properties of all particulates, including polymeric particulates; while they may behave in a fluidlike fashion when they are dry, fluidized and above 100 μm, they also exhibit solidlike behavior, because of the solid–solid interparticle and particle–vessel friction coefficients. The simplest and most common example of the hermaphroditic solid/fluidlike nature of particulates is the pouring of particulates out of a container (fluidlike behavior) onto a flat surface, whereupon they assume a stable-mount, solidlike behavior, shown in Fig. 4.2. This particulate mount supports shear stresses without flowing and, thus by definition, it is a solid. The *angle of repose*, shown below, reflects the static equilibrium between unconfined loose particulates.

Solidlike behavior abounds when the surface-to-volume ratio is very high,[1] that is, when the particulates are even mildly compacted, surface-charged, or wet; all contribute to large frictional forces and to nonuniform, often unstable stress fields in both flowing and compacted particulate assemblies, as we discuss later in this chapter. We begin by discussing some of the unique properties of polymer particulates relevant to processing. Comprehensive reviews can be found in the literature (1–4).

4.1   SOME UNIQUE PROPERTIES OF PARTICULATE SOLIDS

Scientific and engineering investigations into the properties and behavior of particulate solids date back to the early work of Coulomb, who in 1776 developed a theory on "soil pressure and resistance," thus laying sound foundations for important engineering

---

1. Pellets, compared to fine powders, with low surface-to-volume ratios, are readily flowable, easily fluidized and meter- or hopper-fed. These attributes justify pelletization.
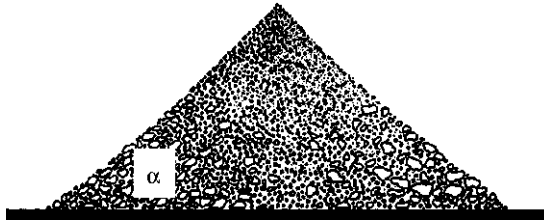
Fig. 4.2   The angle of repose. It should be noted that the angle of repose is generally not a measure of flowability of solids, and as Jenike (22) points out, it is strictly useful only to determine the contour of a pile. Its popularity stems from the ease with which it can be measured.

practices. Later, in 1852, Hagen analyzed the flow of sand in an hourglass, and shortly afterward, Reynolds, in 1885, made his observation on the dilatancy of a deforming mass of sand.[2] The latter, unique property of particulate solids can be observed while walking on wet sand at the seashore. The sand "whitens" or appears to dry momentarily around the foot because the pressure of the foot dilates the sand.

The analysis of particulate solids systems in analogy to fluids can be divided into statics and dynamics: it is interesting to note that, in spite of the early beginnings of scientific interest in the properties of particulate solids, this field—in particular the dynamics of particulate solids—has not experienced the same intensive scientific development as fluid dynamics. In most engineering curricula, relatively little attention is focused on the analysis of particulate solids. Therefore, as engineers, we are generally ill-equipped to analyze these complex systems and to design equipment for handling them, and we may often be surprised by the behavior of solids, such as, for example, the fact that the drag on the plough is independent of its speed (5).

A closer look at the properties of particulate solids and their response to external forces reveals, as pointed out earlier, that these are a blend of (a) liquidlike behavior, (b) solidlike behavior, and (c) particle-interface–dominated behavior, unique to these systems. Like liquids, particulate systems take the shape of the container they occupy, exert pressure on the container walls, and flow through openings. Yet like solids, they support shearing stresses (hence, they form piles), may possess cohesive strength, and exhibit a nonisotropic stress distribution upon application of a unidirectional load. But unlike liquids, shearing stress is proportional to normal load rather than to rate of deformation, and unlike solids, the magnitude of the shearing stress is generally indeterminate, and all that can be said is that the following inequality holds

$$\tau \leq f'\sigma \qquad (4.1\text{-}1)$$

where f' is the interparticle static coefficient of friction and σ represents a range of normal forces ("pressures") that can be applied to the particulate system before a value of shear stress τ is reached that is high enough to start the particles sliding past one another. That is, before particulate solids flow starts, there is a range of equilibrium states and a range of bulk densities allowable. Only at the inception of flow are the frictional forces fully mobilized (4). At this state, the relation takes the form of *Amonton's law*, discussed in the following subsection, which is the defining equation for the coefficient of static friction.

---

2. O. Reynolds, "On Dilatancy of Media Composed of Rigid Particles in Contact. With Experimental Illustrations." *Philos. Mag.*, Ser. 5, **20**, 469 (1885).

Solid–Solid (Dry) Friction

Friction is the tangential resistance offered to the sliding of one solid over another, due to dry friction. Friction is an apparently simple phenomenon with very complex mechanisms that take place on a variety of length scales, from atomic to nano and up. The study of friction is part of the engineering–scientific discipline of *tribology*,[3] which is the scientific study of friction, wear, and lubrication (6). It was Leonardo da Vinci (1452–1519) who discovered the first two laws of friction, namely, that the area of contact has no effect on friction and that friction is proportional to the load. These two laws were rediscovered later by Guillaume Amontons (1663–1705), and later Charles-Augustin Coulomb (1736–1806), added the third law:

1. The friction force (F_T) is directly proportional to the applied load (F_N); that is, $F_T \propto F_N$, where the proportionality constant for any pair of solid surfaces is called the *coefficient of friction*, *f*.
2. The force of friction is independent of the apparent area of contact.
3. Kinetic friction is independent of sliding velocity.

Bowden and Tabor (7) suggested a physical explanation for the observed laws of friction. They determined that the true area of contact is but a small fraction of the apparent area of contact, because the surfaces of even the most highly polished material show irregularities appreciably larger than atomic dimensions called in the literature *asperities*, as shown in Fig. 4.3. Thus, with increasing normal load, more asperities come in contact and the average area of contact grows, as shown in Fig. 4.4

Consequently, Bowden and Tabor (7) specify two factors that are responsible for dry friction: the first, and usually the more important factor, is the adhesion that occurs at the
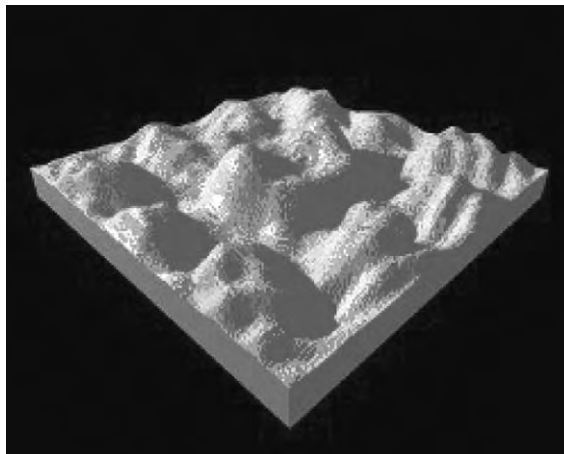

Fig. 4.3   A magnified view of a solid surface showing surface roughness of hills, referred to as asperities, separated by valleys. [Reproduced by permission from I. M. Hutchings, *Tribology: Friction and Wear of Engineering Materials*, Edward Arnold, UK, 1992 (co-published by CRC Press, Boca Raton, FL).]

---

3. The word "tribology" comes from the Greek word $\tau\rho\iota\beta\omega$, which means "to rub."
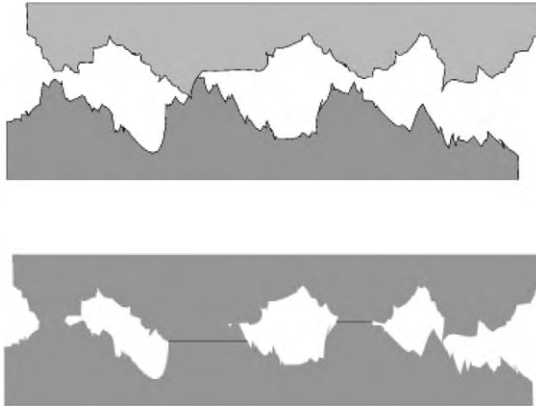
Fig. 4.4   Two surfaces in contact with (a) without normal load, and (b) with normal load.

regions of real contact: these adhesions, welds, or junctions have to be sheared if sliding is to occur; the second factor arises from the plowing and grooving of one surface by the asperities of the other. However, elastic deformation, which precedes the yield point, also plays a role, as does the presence of surface *contaminants*, such as organic compounds or oxides, which tend to decrease adhesion. Disregarding the latter effects, in the case of *static* friction, only adhesion at the contact sites is important, whereas in either sliding or rolling friction, the second factor, plowing, enters the picture. By neglecting the second factor relative to the first, we can approximately explain the first two laws of friction. Because the real contact area is so small, we can assume that, even if the normal load is small, the pressure at the contact points is sufficiently high to reach the value of the yield stress of the softer material σ_y. Assuming that this is indeed the case, that is, that plastic flow occurs, we can argue that the area at a point of contact, A_i is

$$A_i = \frac{F_{N_i}}{\sigma_y} \tag{4.1-2}$$

where F_{Ni} is the load supported by the contact point. An adhering contact point forms a joint that can be broken only when the value of the applied tangential force F_{Ti} reaches the level

$$F_{T_i} = \tau_y \, A_i \tag{4.1-3}$$

where τ_y is the shear strength of the softer material. If we assume that the total tangential frictional force is simply the sum of all, F_{Ti}, we obtain that

$$F_T = \sum F_{T_i} = \frac{\tau_y}{\sigma_y} \sum F_{N_i} = \left(\frac{\tau_y}{\sigma_y}\right) F_N \tag{4.1-4}$$

Equation 4.1-4 suggests that the *static* coefficient of friction is a material property characteristic of the pair of solid surfaces and, specifically, of the softer solid

$$f' = \frac{\tau_y}{\sigma_y} \tag{4.1-5}$$

By extension, Eqs. 4.1-4 and 4.1-5 are assumed to hold for kinematic friction (f), too, assuming that adhesion predominates. The statement that the kinematic friction coefficient

f is a material property, independent of the geometric nature of the surface and frictional process conditions, is only a rough approximation.

Only recent developments in instrumentation of scanning probe microscopy, such as scanning tunneling microscopy (8) and atomic force microscopy (9), have made it possible to study friction on the nanometer and higher scales. These experiments show that the behavior on the single asperity level is different from that on the macroscopic scale.

One of many complications in the experimental studies, and in developing a theoretical foundation, is the interpretation of the experimental results and the complexity caused by ambient conditions, because real surfaces are always contaminated with airborne molecules, water, hydrocarbons, debris, and the formation of liquid bridges. Moreover, sliding of one solid onto another introduces a new set of circumstances and unknowns. It may lead to high and unknown local temperatures and pressures, generating fresh and chemically different surfaces, and mostly altering the topography of the surface as a result of deformation and wear. For these reasons, the coefficients of static and sliding friction are different. The static coefficient is larger than the sliding (kinematic) coefficient. However, recent findings and techniques lend support to Bowden and Tabor's assumption that the macroscopic, dry frictional behavior is undoubtedly dominated by the physics of individual contacts and interactions of contacting asperities (10,11).

In view of these complexities, it is remarkable that Eq. 4.1-4 represents numerous metal–metal, dry frictional data rather well, for both the static and sliding cases. Polymers, on the other hand, exhibit an even more complex frictional behavior on metal. This is, perhaps, not surprising, since the physical situation involves a relatively soft, viscoelastic, and temperature-dependent material in contact with a hard, elastic, and much less temperature- and rate-dependent material. Empirical evidence of these complexities is the nonlinear relationship between the frictional force and the normal load

$$F_T = CF_N^\alpha \qquad (4.1\text{-}6)$$

from which a load-dependent coefficient of friction can be deduced

$$f = CF_N^{\alpha-1} \qquad (4.1\text{-}7)$$

where C is a constant and the exponent α is found to vary between the values of 1 and 0.666. It has been suggested by Lodge and Howell (12) that $\alpha = 2/3$ corresponds to the case of pure elastic deformation at the contact points, whereas $\alpha = 1$, according to Eq. 4.1-4, corresponds to purely plastic (yielding) deformation. Hence, values in between appear to reflect viscoelastic deformation at the contact points. If this is the case, the total contact area would be expected to depend on the normal load, the time of contacts, the temperature, and the speed of sliding. As we shall see later in the chapter, these effects are generally observed. It is worth noting that the expression for the dry coefficient of friction (Eq. 4.1-7) has the same form as that of the viscosity ("internal friction") of a Power Law fluid that describes the non-Newtonian behavior of polymer melts.

From the foregoing it follows that, except for $\alpha = 1$, the coefficient of friction decreases with increasing load, F_N. This observation is a general feature of polymers, namely, that the effective coefficient of friction reduces at higher loads (13,14).

Thus, before we consider the response of particulate systems to externally applied stresses, we must know whether the shear and normal stresses at any point and orientation are above the values specified by the equality of Eq. 4.1-1. Furthermore, since there are two kinds of particulate solids, the noncohesive (free-flowing) and the cohesive, we

comment on the phenomenon of agglomeration, which transforms the former to the latter. Finally, we must remember that, since it is necessary to contain particulate solids, the wall particulate static coefficient of friction and the wall shear and normal forces must be specified. The wall is another location at which flow can be initiated.

4.2   AGGLOMERATION

The term *agglomeration* describes the forming of a cluster of particles from individual particles. Agglomerates form because of the binding of van der Waals forces between individual particles, which require intimate contact to exert any significant attraction. For small particles of sizes up to ultrafine 10 µm, the mass of any one individual particle is so small that it creates a loose-particle agglomeration, and great difficulties in fluidization are encountered. Rotating fluidized beds creating 10–20-g centrifugal fields have recently been used to make the mass of each particulate effectively 10–20 times larger, enabling gas–solid fluidization (15). Presumably, any surface shear stresses imposed on the system have the effect of decreasing the size of agglomerates, either by breakup, or by erosion, or by both (16,17), as is discussed in Chapter 7 in connection with dispersive mixing of solid additives by shear and extensional polymer processing flows. Additionally, solid–solid forces are significantly amplified by increases in pressure exerted on loose particulate assembly regions, leading to "caking." In the processing of particulate-filled polymers, when the particulates and polymer (powder or pellets) are fed as a solid mixture into either single- or twin-rotor processing equipment, compaction takes place in SSEs, and repeated cycles of compressions in TSEs, often leading to caking before melting. Following melting, such agglomerated "cakes" may be held strongly enough for the shearing stresses in the flowing melt to prevent dispersing them. We discuss such a problem in Chapters 9 and 10.

4.3   PRESSURE DISTRIBUTION IN BINS AND HOPPERS

The static pressure under a *liquid column* is isotropic and is determined by the height of the column above the point of measurement, h, and the density of the liquid ρ

$$P = \rho g H \tag{4.3-1}$$

In a column of particulate solids contained in a vertical bin, the pressure at the base will not be proportional to the height of the column because of the friction between the solids and the wall. Moreover, a complex stress distribution develops in the system, which depends on the properties of the particulate solids as well as the loading method. The latter affects the mobilization of friction, both at the wall and within the powder. Finally, *arching* or *doming* may further complicate matters. Hence, an exact solution to the problem is hard to obtain. In 1895, Janssen (18) derived a simple equation for the pressure at the base of the bin, which is still frequently quoted and used. The assumptions that he made are: the vertical compressive stress is constant over any horizontal plane, the ratio of horizontal and vertical stresses is constant and independent of depth, the bulk density is constant, and the wall friction is *fully mobilized*, that is, the powder is in incipient slip condition at the wall.
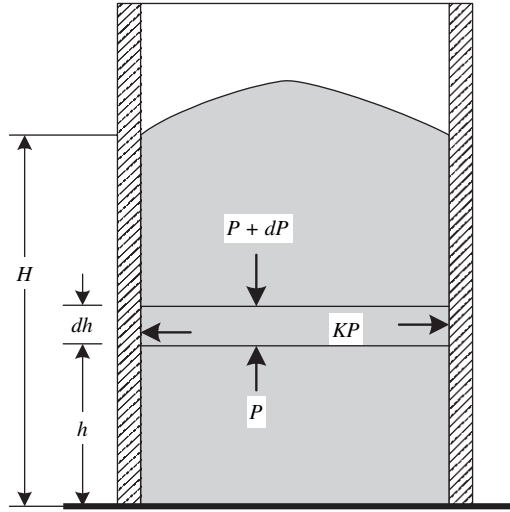
Fig. 4.5 A Vertical bin filled with particulate solids.

A force balance over a differential element (Fig. 4.5) simply using pressure P instead of the compressive stress, with shear stress at the wall $\tau_w = \sigma_w \tan \beta_w + c_w$, where β_w is the angle of internal friction and c_w is the coefficient of cohesion at the wall (14), gives

$$\underset{\substack{\text{[Weight of}\\\text{element]}}}{A\rho_b g\, dh} + \underset{\substack{\text{[Pressure acting}\\\text{downward]}}}{(P+dP)A} = \underset{\substack{\text{[Frictional forces}\\\text{suporting element]}}}{(c_w + f_w' KP)C\, dh} + \underset{\substack{\text{[Pressure acting}\\\text{upward]}}}{PA} \qquad (4.3\text{-}2)$$

where ρ_b is bulk density, A is the cross-sectional area, C the ''wetted'' circumference, and K is the ratio of compressive stress in the horizontal direction to compressive stress in the vertical direction. The physical parameter K is discussed by Tadmor and Gogos (19). Integration of Eq. 4.3-2 results in

$$P = P_1 \left[\frac{f_w' CK(h-h_1)}{A} \right] + \frac{(A\rho_b g/C - c_w)}{f_w' K} \left\{ 1 - \exp\left[\frac{f_w' CK(h-h_1)}{A} \right] \right\} \qquad (4.3\text{-}3)$$

where P_1 is the pressure at height h_1. For the special case of a cylindrical bin, with $h = H$, where $P_1 = 0$ and $c_w = 0$ (no adhesion between solids and the wall), Eq. 4.3-3 reduces to the more familiar Janssen equation

$$P = \frac{\rho_b g D}{4 f_w' K} \left\{ 1 - \exp\left[\frac{4 f_w' K(h-H)}{D} \right] \right\} \qquad (4.3\text{-}4)$$

Clearly the pressure at the base approaches a limiting value as H goes to infinity

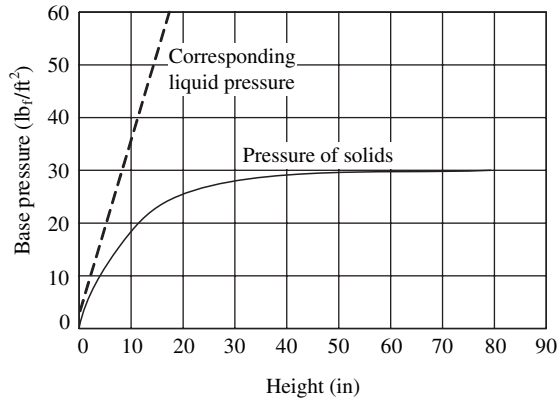$$P_{\max} = \frac{\rho_b g D}{4 f_w' K} \qquad (4.3\text{-}5)$$

Fig. 4.6 Base pressure in a 10-in-diameter cylindrical hopper filled with 1/8-in PS cubes with $K = 0.521, f'_w = 0.523$, and $\rho_b = 39 lb/ft^3$. [Reprinted by permission from W. L. McCabe and J. C. Smith, *Unit Operations of Chemical Engineering*, McGraw-Hill, New York, 1956.]

Hence, most of the weight is supported frictionally by the walls of the bin. The maximum pressure is proportional to bin diameter and inversely proportional to the coefficient of friction at the wall.

Figure 4.6 plots the pressure measured under a load of PS pellets in a 10-in-diameter cylindrical bin as a function of solids height. The many attempts to verify the Janssen equation have met with varying success, and improved models have been offered (20) (these are discussed in some detail in the first edition of this book), but the *shape* of the curve as predicted by the model is usually observed (4). The underlying reason for the good qualitative agreement is that the particulate assembly in the cylindrical hopper is stripped of its volume-wise particle-to-particle interactions, which are due to interparticle friction. The column of particulates is treated as a *solid plug* with only three properties: density, ρ_b; the ratio of the compressive stress in the horizontal direction, K; and the static friction coefficient between the particulates and the hopper wall, f'_w. All these may vary from one location to another, because of neighboring particulate interactions, which include both Newton's second law of motion and a force-deformation constitutive equation for the particulates. The *discrete element method* (DEM), which we discuss in Section 4.10, takes this approach in simulating static and flowing particulate assembly behavior under externally applied and gravity forces.

4.4. FLOW AND FLOW INSTABILITIES IN HOPPERS

In polymer processing practice, we need to ensure that the particulate gravitational mass flow rate of the hopper exceeds, over the complete operating range, the extruder ''open discharge'' rate (i.e., the rate without any die restriction). That is, hoppers must *not* be the production-rate limiting factor. Second, and more importantly, it is necessary for stable extrusion operations and extruded product quality that the flow be steady and free of *instabilities* of the particulate flow emerging from the hoppers. Finally, as we will see in Chapter 9, we need to know the pressure under the hopper in order to determine the pressure profile in a SSE.

There are generally two types of gravitational flow in bins and hoppers [Fig. 4.7(a), 4.7(c)]: ''mass'' flow and ''funnel'' flow. In mass flow, the whole mass of particulate solids
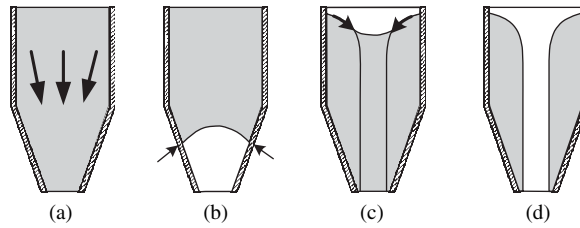
Fig. 4.7 Schematic representation of (a) ''mass'' flow in hoppers, (b) ''arching,'' (c) ''funnel'' flow, and (d) ''piping.''

moves toward the exit, and in funnel flow, the particles flow out through a central opening. In the former, the main cause for flow disturbance is doming or arching, where all the weight of the solids is supported by the walls [Fig. 4.7(b)], whereas in the latter flow, disturbances may occur when the solids can sustain the existence of an empty central tube, called '*piping*' [Fig. 4.7(d)]. These and other flow disturbances were discussed by Johanson (21). In both arching and piping, the solids must have consolidated sufficiently to develop the level of strength necessary to sustain the weight of the retained particulate solids. Hence, obstruction to flow is acute in cohesive particulate solids and it depends, in addition to material properties, on hopper geometry, which determines the stress distribution in the system. Jenike (22) and Richmond and Gardner (23), among others, developed design methods and criteria for building obstruction-free hoppers and bins.
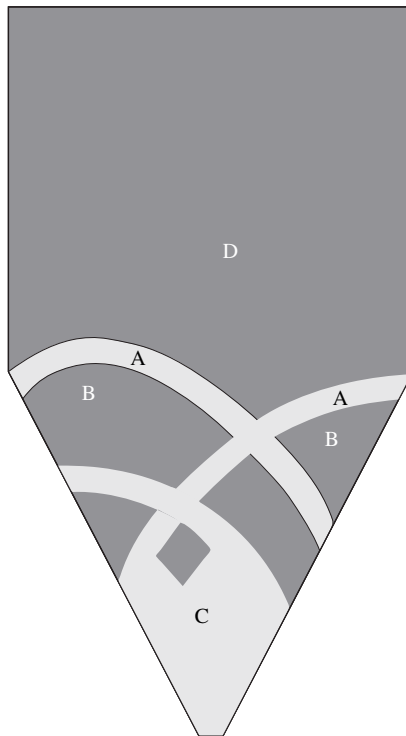

Fig. 4.8 Regions of different flow behavior in two-dimensional hoppers as observed by radiographic techniques. [Reprinted by permission from J. Lee et al., *Trans. Soc. Rheol.*, **18**, 247 (1974).]

The flow pattern in two-dimensional hoppers was studied by Lee et al. (24). They used radiographic techniques to determine simultaneously the flow field and the porosity field. The marks left by tracer particles during discharge permit the evaluation of the local velocity vector, and the intensity of the shade, the porosity. On the basis of both velocity and porosity fields, the authors distinguished between four regions (Fig. 4.8): region D they identified as a "plug-flow zone"; in region B they observed rigid-body behavior; region A appeared to be a "rupture zone," where intensive deformation occurs, and region C is a free-flow zone. A detailed mapping of the flow kinematics in two-dimensional hoppers using the stereoscopic technique developed by Butterfield et al. (25), was done by Levinson et al. (26). Other noninvasive techniques such as MRI were applied more recently to the study of the flow fields in particulate systems (27,28).

Although a great deal of progress has been made in obtaining flow fields of particulate solids, and design criteria for arch-free flow are available, it is not yet possible to calculate discharge rates from first principles. Hence, empirical equations are used for this purpose. It should be noted, perhaps, that in most polymer processing applications, such as in hopper feeding processing equipment, the maximum, open discharge hopper flow rates are much higher than present processing rates. This was aptly shown in a recent paper by Potente and Pohl (29), where it is shown that hoppers can become limiting (because of flight interference to hopper flows) only at very high screw speeds.

4.5   COMPACTION

The response of particulate solid systems, specifically powders, to forced compaction, is of great interest in a broad range of processes. *Tableting* or *pelleting* of pharmaceutical products, powder pressing in ceramic industries, powder metallurgy, and briquetting of coal can serve as examples. In polymer processing, loose particulate solids are compacted prior to melting inside most processing machinery, and the performance of these machines is greatly influenced by the compaction behavior of the solids.

In polymer processing, compaction is an important and necessary step in order to reduce the interparticle, unoccupied spaces and thus eliminate air. It is essential for melting in both single-screw extruders as well as for twin-rotor processors, as we shall see in Chapters 5 and 10. In twin-rotor devices, such as Co-TSEs, for example, the large and repeated deformation of *compacted* particulates by the "kneading elements," which induces large *plastic* deformation of particulates, is the dominant melting mechanism.

In other applications, the purpose of compaction is to induce agglomeration. The compaction is obtained by applying an external force. This force is transmitted within the system through the points of contact between the particles. By a process of small elastic and plastic deformation (shear deformation and local failure), the points of contact increase, as do the forces holding the particles together, as discussed in the section dealing with agglomeration. The externally applied force generates an internal stress field, which, in turn, determines the compaction behavior.

It was Wollaston (30) who in 1829 recognized the great pressures needed for compaction of dry powders—an observation that led to his famous toggle press. Since that time, compaction and deformation of powders and particulate systems have been extensively studied (31–35). There are many difficulties in analyzing the compaction process. Troublesome in particular are the facts that the properties of particulate solids vary greatly with consolidation, and that stress fields can be obtained, in principle, only in
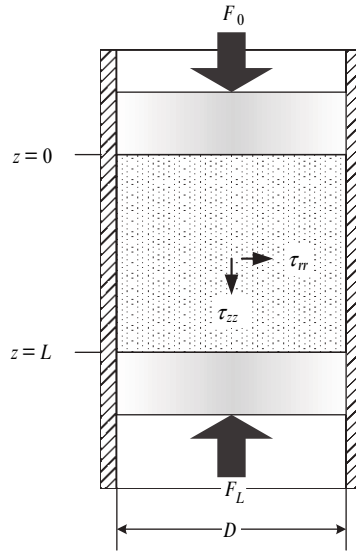
Fig. 4.9 Compaction in a cylindrical channel, between frictionless pistons. F_0 is the applied force, F_L is the resultant force on the lower portion.

the limiting cases of steady flow or in a state of incipient flow when the friction is fully mobilized. In compaction, these conditions are not necessarily fulfilled.

Let us consider an apparently simple situation of compaction of solids in a cylinder (Fig. 4.9). Assuming a uniform stress field, a normal force F_0 applied to the top ram generates within the solids a certain normal stress τ_{zz}, as well as a radial stress τ_{rr}. The frictional shear force due to the latter acts in the opposite direction to the applied force. Hence, the transmitted force to the lower ram, F_L, will be smaller than the applied force. By making a force balance similar to that made in deriving the Janssen equation, and assuming that the wall friction is fully mobilized, that the ratio of axial to radial stresses is a constant throughout, and that the coefficient of friction at the wall is constant, we obtain the following simple exponential relationship between the applied and transmitted force:

$$\frac{F_0}{F_L} = \exp\left(\frac{4f_w' KL}{D}\right) \tag{4.5-1}$$

Experimental data seem to conform to this relationship, yet there are serious doubts about its validity. Both the coefficient of friction and the ratio of normal stresses vary along the compaction (although it appears that their product stays approximately constant, explaining the reasonable agreement with experimental data). Experimental measurement of stresses within the compaction, however, reveal a rather complex stress distribution (31), which depends very much on conditions at the wall and the geometry of the compaction, as shown in Fig. 4.10.

Another question of fundamental importance discussed by Long (33) is the nature of the ratio of axial to radial stresses. Since there is complex stress distribution, the principal axes may not coincide with the axial and radial directions, respectively. Long (33) investigated this relationship by carrying out "radial stress cycles." The cycles are
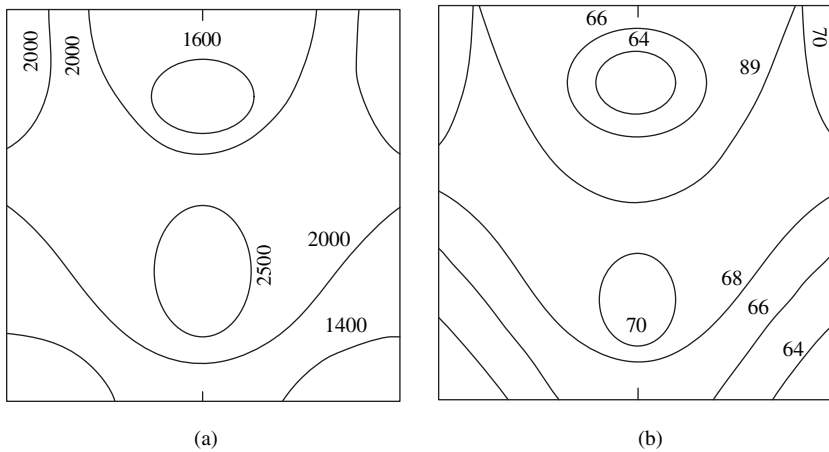
Fig. 4.10 (a) Stress and (b) density distribution in a cylindrical compaction of magnesium carbonate at an applied pressure of 2040 kg/cm^2. [Reprinted by permission from D. Train, *Trans. Inst. Chem. Eng.*, **35**, 262 (1957).]

obtained by first increasing the axial stress, then decreasing it. A residual radial stress remains after the axial stress has been reduced to zero. This residual stress is responsible for the necessity of forcing the compacted mass out from the die after removal of the axial stress. According to Long, at small axial stresses, before any yield takes place in the powder, the ratio of radial to axial stresses will be given by the Poisson ratio, v, which is the stress needed to suppress the radial expansion the compact would undergo if it were free to expand. However, once yield takes place, the ratio is determined by some yield criterion such as the Coulomb yield function (19), and a more or less linear increase of radial stress with axial stress is observed.

The response of polymeric particulate solids to compaction was investigated experimentally by Schneider (36) and Goldacker (37). For polyethylene, for example, a constant radial-to-axial stress ratio of 0.4 was observed.

The bulk density of particulate solids increases by compaction. Dilation, mentioned earlier, occurs only in the presence of a free surface, which allows for a loosening of the packing arrangements of the particles. The increase in density, or decrease in porosity, seems to follow an exponential relationship with the applied pressure (38,39)

$$\varepsilon = \varepsilon_0 e^{-\beta' P} \tag{4.5-2}$$

where ε_0 is the porosity at $P = 0$, and β' is a "compressibility coefficient," which, in view of the complex stress distribution in compacts, should depend on properties of the particulate system, on compact geometry, and possibly on the loading history. Therefore, Eq. 4.5-2 can be viewed as an approximate empirical relationship reflecting some average values. The inability to quantitatively describe or predict the internal stresses and deformations of particulate assemblies under static or dynamic loads, and the velocity fields of flowing particulates, has led to the rapidly growing development and use of the numerical method, which is uniquely appropriate for the discreet nature of particulate assemblies.

4.6   FLOW IN CLOSED CONDUITS

In polymer processing, it is usually necessary to force the particulate solids through some sort of closed conduit or channel. In a ram-type injection molding machine, the solids are pushed forward by the advancing ram. They move in a channel that becomes an annular gap upon reaching the torpedo. In a screw extruder, the solids get compacted and *dragged* forward in the helical channel formed between the screw and the barrel. These examples represent the two basic conveying and compaction methods used in polymer processing: external, mechanical, positive displacement conveying and compaction, and drag-induced conveying and compaction by a solid boundary in the direction of flow. In the former, the friction between the solids and the stationary walls reduces the conveying capacity, whereas in the latter, friction between the solids and the moving wall is the *source* of the driving force for conveying. It is perhaps worthwhile to note that the two solids-conveying mechanisms are identical in concept to external mechanical pressurization and drag-induced, viscous pressurization of liquids, discussed in Chapter 6.

Rigorous analysis of the flow of compacted particulate solids in closed conduits is difficult, as we discussed earlier. Discreet numerical methods such as DEM, which is discussed in Section 4.10, offer the promise of more rigorous analysis, but these methods are also subject to severe limitations related to small elastic deformations and relatively simple channel geometries. Moreover, the difficulties with using DEM are compounded by the complexities of polymer processing, such as temperature increases as a result of friction and external heating, and the viscoelastic response of polymeric particulate systems under externally applied forces. Thus, despite the very serious doubts as to the validity of the conventional assumptions that compacted particulate systems can be analyzed as a continuum, often referred to as a *solid plug*, which is devoid of internal local assembly rearrangements and deformations, the '*solid-plug*' *assumption* is widely used in polymer processing modeling. We therefore analyze the following three modes of particulate flows next: mechanical-displacement flow (Section 4.7), steady mechanical-displacement flow aided by frictional drag (Section 4.8), and steady, drag-induced flow in a straight channel (Section 4.9). These are really not flows as we refer to them in fluid mechanics, but rather transport of slightly compressible but otherwise nondeformable plugs.

4.7   MECHANICAL DISPLACEMENT FLOW

We now analyze mechanical-displacement flow in a straight channel of constant cross-sectional area, as shown in Fig. 4.11 (with the upper plate at rest). A column of compacted solids of length L is compressed between two rams. The one on the left exerts a force F_0 on the solids and it is opposed by a smaller force F_L on the right. Thus, friction on the channel walls also opposes the applied resultant force.

A differential force balance with the following assumptions: (a) the compacted solids are either at a steady motion or in a state of incipient slip on the wall (friction at the wall is fully mobilized); (b) axial and radial stresses vary only with the axial distance x; (c) the ratio of the radial-to-axial stresses is a constant K, independent of location; (d) the coefficient of friction is constant and independent of compaction; and (e) temperature effects in the case of steady motion are negligible, results in

$$F_x - (F_x + dF_x) - C\left(\frac{F_x}{A}\right) K f_i \, dx = 0 \qquad (4.7\text{-}1)$$
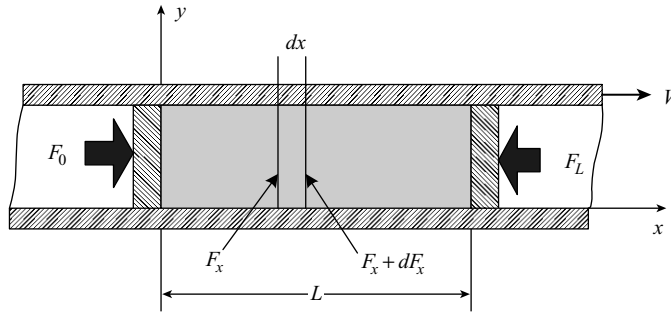
Fig. 4.11   A column of particulate solids compressed between two pistons in a channel with a constant cross section. A force F_0 is applied at $x = 0$, which is balanced by a force F_L at $x = L$. The column is either moving at constant velocity or is stationary. The upper plate is either stationary or is moving with constant velocity.

where f_i is either the static coefficient of friction for the case of incipient motion, or the kinematic coefficient of friction for steady motion; C is the circumference, which for noncircular cross sections is the wetted perimeter; and A is the cross-sectional area.

Integration of Eq. 4.7.1 gives

$$F_x = F_0 e^{-f_i K C x / A} \tag{4.7-2}$$

where F_x is the axial force at location x. The axial stress may be obtained by multiplying the force by the cross-sectional area. The force at the downstream ram F_L is obtained by setting $x = L$ in Eq. 4.7-2.

Hence, in dealing with steady motion of particulate solids, it is evident that the axial stress or "pressure" drops *exponentially*, whereas in the case of liquid flow, it drops *linearly* with distance. This difference stems, of course, from the fact that frictional forces on the wall are proportional to the absolute local value of normal stress or pressure. In liquids, only the pressure gradient and not the absolute value of the pressure affects the flow. Furthermore, Eq. 4.7.2 indicates that the pushing force increases exponentially with the coefficient of friction and with the geometric, dimensionless group CL/A, which for a tubular conduit becomes $4 L/D$.

Experimental support on the validity of Eq. 4.7-2 was presented by Spencer et al. (32), who also proposed a theoretical derivation based on considering a discrete number of contact points between solids and containing walls. They assumed isotropic stress distribution ($K = 1$) and obtained an expression identical to Eq. 4.7-2

$$\frac{F_L}{F_0} = e^{-4 f'_w L_0 / D} \tag{4.7-3}$$

where L_0 is the initial length of the column. The use of initial length of column, even though the column shortens upon compression, is justified by Spencer et al. on the basis of assuming a constant number of contact points. Experiments were carried out with a stationary column of saran powders and granular polystyrene, and results confirmed the theoretical derivation within experimental error.

Example 4.1   Force Requirements of Ram Injection Molding Machines   We consider a ram injection-molding machine consisting of a 2-in-diameter barrel in which a well-fitting

ram reciprocates. We wish to calculate the maximum length of the solid plug the machine can deliver if the downstream pressure during injection is 10,000 psi and the barrel can sustain a radial stress of 25,000 psi. The static coefficient of friction is 0.5, and the radial-to-axial stress ratio is 0.4.

With a 25,000-psi allowed radial stress, the maximum allowable axial stress is $25,000/0.4 = 62,500$ psi. Substituting the appropriate values into Eq. 4.7-3, but not setting $K = 1$, we get

$$\ln(6.25) = (0.5)(0.4)(4)\frac{L}{2}$$

The length L is 4.58 in. Thus with an axial force of about 20,000 lb, we can only press a 4.58-in-long solids column driving the radial stress to its upper limit! Clearly, if it is necessary for injection molding machines of this type to develop such high downstream pressures, appropriate means must be provided to reduce the coefficient of friction on the wall. This can be achieved, for example, by heating the barrel, generating a liquid film on the wall. This will change the drag mechanism to that of a viscous laminar flow, which is independent of the absolute local normal stresses.

4.8   STEADY MECHANICAL DISPLACEMENT FLOW AIDED BY DRAG

Drag-aided, particulate solids flow occurs when at least one of the confining solid walls moves in the direction of flow parallel to its plane. The friction between the moving wall and the solids exerts a forward dragging force on the solids. Figure 4.11 shows a rectangular channel with the upper plate, which forms the top of the channel, moving at a constant velocity in the x direction. Particulate solids are compressed into a column of length L between two rams. We now can differentiate between four possible states of equilibrium:

a. The solids are stationary with friction on the stationary walls fully mobilized, and with $F_0 > F_L$.
b. The same as Case 1, but with $F_L > F_0$.
c. The solids move at constant velocity (less than the velocity of the upper plate) in the positive x direction.
d. The same as Case 3, but the solids move in the negative x direction.

Force balances on a differential element for these four cases appear in Fig. 4.12. The moving plate exerts a force of $C_1 f_{w1} K(F/A)$ in all cases, where C_1 is the portion of the "wetted" perimeter of the moving plate and f_{w1} is the kinematic coefficient of friction. The stationary channel walls in Cases (a) and (b) exert a force $C_2 f'_w K(F/A)$, where f'_w is the static coefficient of friction and C_2 is the portion of the wetted perimeter of the lower plate and side walls that is stationary. This force points in the direction of increasing force. Thus it points to the left in Case (a) and to the right in Case (b).

Finally in Cases (c) and (d), the stationary walls exert a force $C_2 f_{w2} K(F/A)$, where f_{w2} is the kinematic coefficient of friction. This force acts in the direction opposite to the direction of motion of the plug.
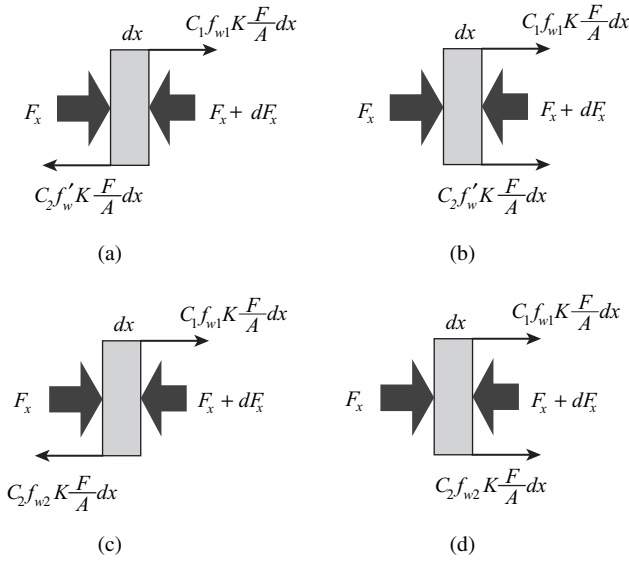
Fig. 4.12 Force balances on a differential element of solids in Fig. 4.11. (a) Stationary solids $F_0 > F_L$; (b) Stationary solids, $F_0 < F_L$; (c) Solids move at constant velocity in the positive x direction. (d) Solids move at constant velocity in the negative x direction.

Force balances such as Eq. 4.7.1, with the further assumption that the channel is flat and the torque induced by couples of forces can be neglected, lead to the following equations.

Case a $F_L < F_0$: Stationary plug; friction mobilized:

$$\frac{F_L}{F_0} = \exp\left[(C_1 f_{w1} - C_2 f'_w)\frac{KL}{A}\right] \tag{4.8-1}$$

Case b $F_L > F_0$: Stationary plug; friction mobilized:

$$\frac{F_L}{F_0} = \exp\left[(C_1 f_{w1} + C_2 f'_w)\frac{KL}{A}\right] \tag{4.8-2}$$

Case c   Plug moves in the direction of the upper plate:

$$\frac{F_L}{F_0} = \exp\left[(C_1 f_{w1} - C_2 f_{w2})\frac{KL}{A}\right] \tag{4.8-3}$$

Case d   Plug moves in the direction opposite to the upper plate $(F_L > F_0)$:

$$\frac{F_L}{F_0} = \exp\left[(C_1 f_{w1} + C_2 f_{w2})\frac{KL}{A}\right] \tag{4.8-4}$$

In the foregoing, we have allowed for different kinematic coefficients of friction on the moving plate f_{w1} and the stationary walls f_{w2}.

Analysis of these equations reveals the role of drag on the force and stress distribution. First, we consider the case of a stationary column of solids. Assume that the drag force
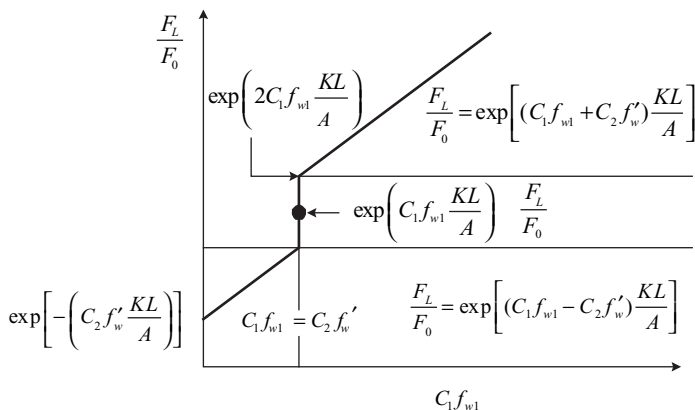
Fig. 4.13 The effect of drag on the ratio F_L/F_0 for a stationary column of solids. (The ordinate is a logarithmic scale.)

exerted by the moving plate can be gradually increased by changing $f_{w1}C_1$, by modifying the surface properties of the plate through coating, roughening, and so on, or increasing C_1. This is demonstrated graphically in Fig. 4.13.

If $f_{w1}C_1$ is zero, the ratio of the forces is $F_L/F_0 = \exp[(-C_2 f'_w)KL/A]$, as given in Eq. 4.7-2. A gradual increase in $f_{w1}C_1$ increases this ratio, implying that, for a given F_L, less and less force has to be exerted on the upstream ram, until this ratio reaches a value of 1 (i.e., $F_L = F_0$) when $C_1 f_{w1} = C_2 f'_w$. At this point, the forward dragging force exerted by the upper plate exactly compensates the fully mobilized frictional forces on the stationary walls. Now we can slightly increase F_L, thereby demobilizing the friction on the stationary walls. This is indicated by the vertical line in Fig. 4.14. We then reach a point where the frictional forces on the stationary plate are zero and the forward dragging force is fully compensated by the force F_L Under these conditions

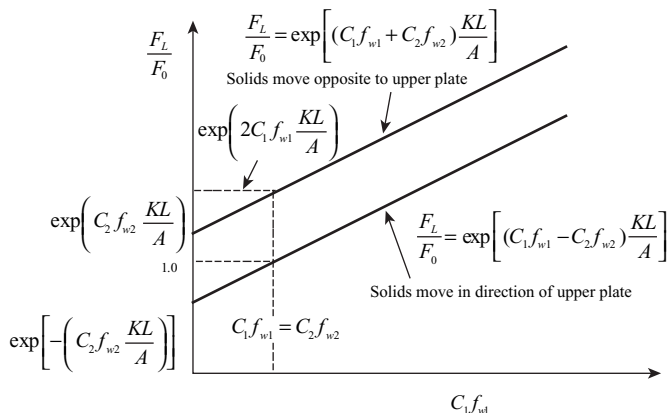$$\frac{F_L}{F_0} = \exp\left(C_1 f_{w1} \frac{KL}{A} \right) \tag{4.8-5}$$

Fig. 4.14 The effect of drag on the ratio F_L/F_0 for a steadily moving column of solids. (The ordinate is a logarithmic scale.)

which is indicated by the heavy dot in Fig. 4.13. The force F_L *can* gradually be further increased, mobilizing the frictional forces on the stationary walls in the opposite direction until they are fully mobilized, where the ratio of forces is

$$\frac{F_L}{F_0} = \exp\left(2C_1 f_{w1} \frac{KL}{A}\right) \tag{4.8-6}$$

A further increase in $f_{w1} C_1$ will result in an increase in the ratio F_L/F_0 according to Eq. 4.8-2. Analyzing the whole curve, we see that we have a condition indicated by the vertical line in Fig. 4.13, where the force ratio is indeterminate. The condition indicated by the heavy dot on the vertical line can also be interpreted as representing a point where the downstream ram is replaced by a rigid channel block, which responds only to the forces exerted on it by the solids and prevents mobilizing the friction on the stationary walls. This is in agreement with the St. Venant principle, which states that, if statically equivalent and opposing surface tractions are applied on a solid, the differences are negligible at far away locations, that is, on the surface of the stationary walls; hence, this surface plays no role in the force balance.

The same kind of analysis for the case of steadily moving solids leads to similar conclusions, as Fig. 4.14 demonstrates. We should note, though, that in this case, we do not have a continuous transition between the two directions of motion, because within the region between the two curves, the solids must come to rest, thus encountering the two previously discussed cases and leading to possible instabilities.

Both cases, however, vividly demonstrate the profound effect that drag forces, induced by a moving boundary, may have on the force distribution. In positive displacement flow, the addition of a drag permits the reduction of the force F_0 needed to maintain a certain downstream force F_L to any desired level. Moreover, results indicate that drag is capable of generating pressures within the solids above those applied externally. The pressure rise is exponential with distance. The same holds for a moving plug. Hence drag, as we shall see in the next section, is a mechanism by which solids can be compacted as well as conveyed.

4.9   STEADY DRAG-INDUCED FLOW IN STRAIGHT CHANNELS

We have concluded that frictional drag, when applied to a steadily moving column of solids, can generate stresses or pressures above those applied externally. Consider once more the case of a flat rectangular channel with the upper plate moving and the solids moving in the same direction at constant velocity. The force ratio is plotted in the lower curve of Fig. 4.14. Clearly, for any given F_0 (which must be greater than zero, except for the frictionless case), we can get any F_L greater than F_0, provided $C_1 f_{w1}$ is large enough. This ratio F_L/F_0 seems to be independent of either the plate velocity or the velocity of the solids. All that is required is that these velocities be steady. This result was obtained because we have assumed that the frictional force depends only on normal stress and is independent of velocity, which, as we have seen in this chapter, is a reasonable assumption. Yet the velocity of the solids multiplied by the cross-sectional area gives the flow rate. Thus the previous argument implies that, in this particular setup, flow rate is indeterminate. How, then, can we use the drag-induced flow concept to obtain a geometrical configuration in which flow rate is not only indeterminate but is also predictable? Such a situation would arise if the frictional drag could be made dependent on solids velocity. We can create such a situation by replacing the upper cover
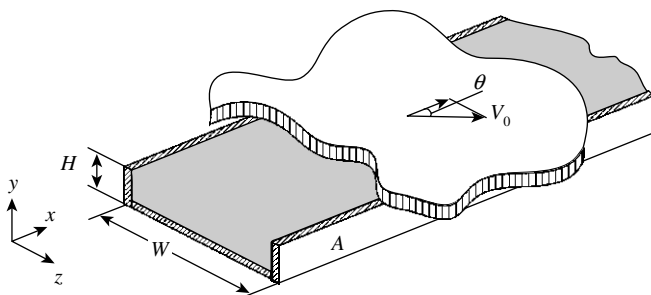
Fig. 4.15 A rectangular channel filled with solids that move in the positive x direction at constant velocity u, covered by an infinite plate moving at constant velocity V_0 at an angle θ to the down-channel direction, z.

plate with an infinite plate, moving not in the down-channel direction, but at an angle, θ, to this direction, as in Fig. 4.15.

The frictional force exerted by the moving plate on the solids remains constant, but the direction of this force will be given by the vectorial difference between the plate velocity and solids velocity (Fig. 4.16). Hence, the velocity component of this force in the down-channel direction, which participates in the force balance, becomes a function of both plate velocity and solids velocity (or flow rate). From the velocity diagram in Fig. 4.16, we obtain the following expression for the angle ϕ, which is the angle between the direction of the force exerted by the moving plate on the solids and the direction of motion of the moving plate (the solids conveying angle) where

$$\tan \phi = \frac{u \sin \theta}{V_0 - u \cos \theta} \tag{4.9-1}$$

where V_0 is the velocity of the upper plate, and u is the velocity of the solids. Note that, for stationary solids, the angle ϕ becomes zero, and it increases with increasing flow rate.

Next we can proceed with the force balance on the differential element shown in Fig. 4.16. We first concentrate on making a down-channel force balance, neglecting the cross-channel component of the forces

$$F_x - (F_x + dF_x) + C_1 f_{w1} K \left(\frac{F_x}{A}\right) \cos(\theta + \phi)\, dx - C_2 f_{w2} K \left(\frac{F_x}{A}\right) dx = 0 \tag{4.9-2}$$
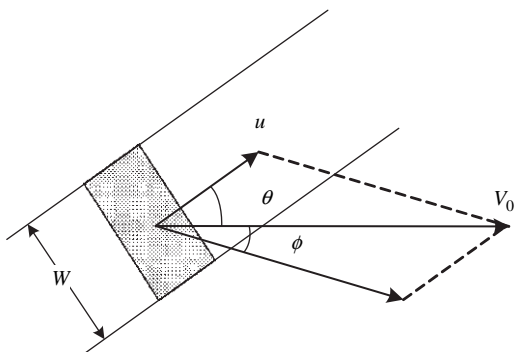

Fig. 4.16 Top view of a differential element of the column of solids in Fig. 4.15.

which upon integration with the initial condition $F(0) = F_0$, gives

$$\frac{P_x}{P_0} = \frac{F_x}{F_0} = \exp\left\{[C_1 f_{w1} \cos(\theta + \phi) - C_2 f_{w2}]\frac{Kx}{A}\right\} \tag{4.9-3}$$

Hence the ratio of forces, which by dividing by the cross-sectional area also equals the ratio of axial stresses, which we shall refer to as *pressures*, become a function of the flow rate via the angle ϕ determined by Eq. 4.9-1. This implies that, for a given inlet pressure P_0, a fixed outlet pressure determines the flow rate, or conversely, a given flow rate determines the magnitude of outlet pressure the device can generate. The lower the flow rate, the higher the pressure rise.

The previously described solids conveying mechanism represents, in essence, the conveying of solids in SSEs, although a realistic conveying model for the latter is somewhat more complicated because, as Chapter 9 explains, the channel is curved.

Drag-induced flow in a rectangular channel, as in Fig. 4.15, neglecting cross-channel forces, resulted in Eq. 4.9-3. We now consider the effect of these forces on the conveying mechanism.

At steady flow conditions the moving plate exerts a force on the solids in the $(\theta + \phi)$ direction. This force is separated into two components: one in the down-channel direction, which was used in the force balance, and the other in the cross-channel direction, which was neglected. The latter will have the following effects: it will increase the normal stress on the side wall, A, in Fig. 4.15, and it will alter the stress distribution within the solids. Assume for the sake of simplicity that the St. Venant principle holds, that is, the externally applied force by the plate is completely balanced by the additional force on the side wall A, and within the solids (which will be considered to be located "far" from the places where these tractions act), there will be no effect. In other words, we neglect the changes in the stress distribution within the solids. The cross-channel force component, F^*, is

$$F^* = f_{w1}K\left(\frac{F_x}{HW}\right)(W\,dx)\sin(\theta + \phi) = \frac{f_{w1}KF_x \sin(\theta + \phi)\,dx}{H} \tag{4.9-4}$$

where W and H are the width and height of the channels, respectively. Now we can write a down-channel force balance, including the effect of this additional normal force on side wall A on the frictional force along this wall

$$F_x - (F_x + dF_x) + f_{w1}K\left(\frac{F_x}{HW}\right)(W\,dx)\cos(\theta + \phi) - f_{w2}K\left(\frac{F_x}{HW}\right)(W + H)\,dx$$
$$- f_{w2}\left[K\left(\frac{F_x}{HW}\right)H\,dx + F^*\right] = 0 \tag{4.9-5}$$

which, upon rearrangement and with Eq. 4.9-4, gives

$$\frac{dF_x}{F_x} = \frac{f_{w1}K}{H}\left[\cos(\theta + \phi) - \frac{f_{w2}}{f_{w1}}\left(1 + 2\frac{H}{W}\right) - f_{w2}\sin(\theta + \phi)\right]dx \tag{4.9-6}$$

Integration of this equation gives

$$\frac{P_x}{P_0} = \frac{F_x}{F_0} = \exp\left\{\frac{f_{w1}Kx[\cos(\theta + \phi) - f_{w2}\sin(\theta + \phi) - f_{w2}/f_{w1}(1 + 2H/W)]}{H}\right\} \tag{4.9-7}$$

Equation 4.9-7 reduces to Eq. 4.9-3 if the second term on the right-hand side vanishes. Clearly the cross-channel force induces additional friction on the side wall, A, which in turn reduces the pressure generation capability for a given flow rate (given angle ϕ), or it reduces the conveying capacity for a given pressure rise.

4.10   THE DISCRETE ELEMENT METHOD

In Sections 4.4 and 4.5, we dealt briefly with particulate flow instabilities in hoppers and the nonhomogeneous stress distributions created under uniaxial loading of a particulate assembly. In this section, we will expand on the *discrete* nature of such assemblies, and refer the reader to the computational and experimental tools that have been developed, and are rapidly advancing, to study such phenomena.

An assembly of particulates is composed of distinct particles that undergo displacements independently from each other, and interact only via *points of contact* between the particles. This *discrete* character of such assemblies results in complex behavior under loading and unloading, as well as under flow, which the available, continuum-based constitutive equations fail to describe. In this section we describe particle dynamics simulations, which are based on the discreet, rather than the continuum nature of particulates, and which offer a better chance to describe the behavior of such systems. Experimentally, it is very difficult to measure internal stresses or flow details in real particulate assemblies. Thus, "model" experimental systems have to be used, which consist of assemblies of geometrically simpler "particles." For example, DeJosselin de Jong and Verrijt in 1971 (40) used a two-dimensional assembly of photoelastic disks of various sizes under load. Figure 4.17(a), taken from their work, records the "force vector" plots resulting from the two-dimensional loading, and Fig. 4.17(b) shows a simulation by Cundall and Strack (41). The complex stress field is evident where the width of the lines indicates the magnitude of the force.

Relatively simple optical experimental techniques to study *noncohesive* particulate flow have also been developed, such as the polarized light probe system by Allersma (42,43). With this technique, the principal stress distribution and displacement of photoelastic granular material flowing in two-dimensional hoppers, with and without obstructions (distribution bars), can be obtained, as shown in Fig. 4.18.
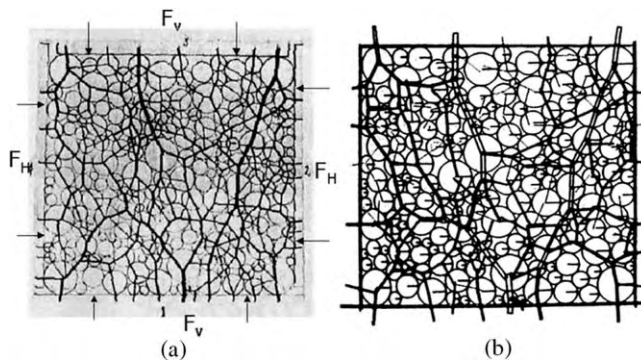

Fig. 4.17   (a) Force vectors obtained in a two-dimensional assembly of photoelastic disks under horizontal and vertical loads, $F_H/F_V = 0.39$. (b) DEM calculations by Cundall and Strack (41) of the force vectors for $F_H/F_V = 0.41$ [Reprinted by permission from P. A Cundall and O. D. L Strack, "A Distinct Element Model for Granular Assemblies," *Géotechnique*, **29**, 47–65 (1979).]
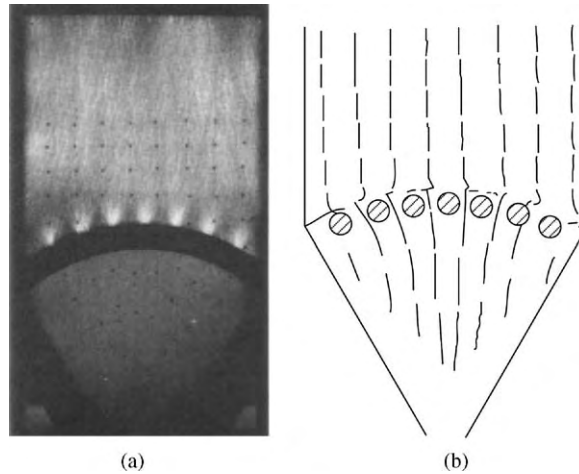
Fig. 4.18   (a) The visualized stress distribution in a hopper with seven distribution bars. (b) The measured particle displacements in the same hopper indicating uniform flow. [Reprinted by permission from H. G. B. Allersma "Optical Analysis of Methods to Influence the Stress Distribution in Hoppers," in *Mechanics of Deformation and Flow of Particulate Materials*, C. S. Chang et al. Eds., ASCE Publication, New York, 1997.]

Altobelli et al., used a more elaborate three-dimensional MRI technique to study the flow of suspended particles (44) and granular flows (27), also studied by Ng et al. (45) for pellet-sized pills under load, while being sheared in a nonmagnetic "shear box," similar to the Jenicke cell (22). This technique holds great potential for detecting details of particulate movements and deformations of three-dimensional particulate assemblies, but is currently limited to very low shearing velocities.

In the last decades, the modeling of both compacted particulates and flowing particle assemblies under loads and under flow conditions has been advanced by DEM, first developed by Cundall (46) for two-dimensional compacted-disk assemblies in 1971. The origins of DEM are in the field of molecular dynamics (MD), where the motions of individual molecules are tracked under the influence of an external force (e.g., electrostatic) field (47). Experimental results such as those with model photo-elastic assemblies just discussed have also assisted the development of the DEM simulation models.

In a dynamic particulate assembly, particle–particle interactions dominate. Thus, it is essential for DEM to establish methods for identifying contacts and modeling the contact interactions for all particulates. Most DEM simulations assume that the particles are spheres, to facilitate the identification of the contact location. There are two categories of DEM: the hard-(infinitely rigid) sphere model and the soft-sphere model. The hard-sphere model is appropriate for sparse populations of bodies moving at high speeds, with instantaneous two-body collisions only, which can be modeled as instantaneous exchanges of momentum and energy (48). Haff (49) discusses the physical nature of such binary, collision-dominated systems, resembling gases, but where the collisions are allowed to be *inelastic* in the transfer of momentum and energy. He derives, heuristically, the equation of state and the momentum and energy balances for such systems. This model, however, is not applicable to dense particulate flows and deformation of packed particulates under loads, relevant to polymer particulate solids handling.

On the other hand, in Cundall's soft-sphere model of the DEM, "soft" spheres colliding, or in contact with several neighboring particles, undergo virtual (overlap) deformations, which give rise to reaction (e.g., elastic, springlike) forces normal and tangential to the contact. Thus, each contact can exert both a force and a moment on each particle, the total of which is the resultant of all the contacts and the body forces of gravity and electrostatic fields, if any. The new positions and velocities of each particle are determined by Newton's second law and solving second order differential equations involving the linear and angular acceleration of each particle. The simultaneous solution of the entire assembly differential equations determines the new "state" of the assembly. Figure 4.19 shows the computational flow diagram of the soft-sphere DEM model. It is important to note that this DEM model is equally applicable to static, quasi-static, and dynamic flow conditions.

We follow Cundall and Strack (41) in discussing this DEM model in two-dimensional assemblies of disks under load. The equilibrium contact forces and particle displacements and deformations of a stressed assembly of disks are predicted through a series of calculations tracing the dynamic state of each particle, which is the result of the propagation, through the assembly, of the externally applied wall stresses. Calculations are carried out in sequential, small time increments over which we can assume that the particle velocities and accelerations are constant. The time steps are also small enough so that disk-to-disk interactions (disturbances) have the time to propagate only to immediate "neighbors" and no further. Thus, at all times during the calculations, the resulting forces on any disk are determined only by its interactions with the neighbors it is in contact with. This is the essential computational component that enables DEM to follow nonlinear interactions between very large numbers of district disks, with moderate computer memory requirements.
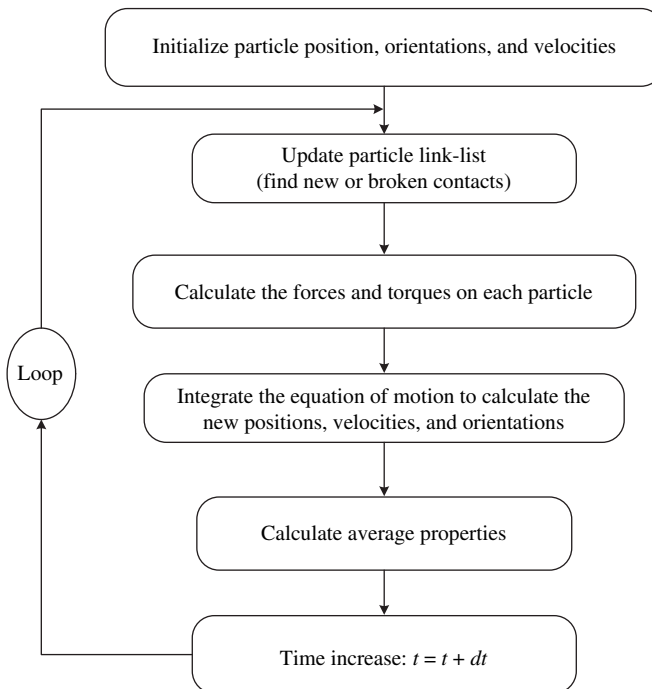

Fig. 4.19 The computational algorithm of the soft-sphere DEM model.

The DEM calculation cycle (as noted in Fig. 4.19) involves the use of Newton's second law, giving the motion of a particle resulting from the forces acting on it, alternating with the use of a force-displacement (particle deformation) constitutive relationship to find contact forces from displacements. The deformations of individual soft particles are "virtual" in the sense that they are used only to calculate reaction forces. The response and deformation of the entire assembly is calculated by the displacements and the rigid-body rotation of all particles. This assumption limits the applicability of the soft-sphere DEM to the description of the dynamic state of packed polymer pellets or powders in processing equipment, such as twin rotor processing equipment, as we will discuss in Section 5.8 and Chapter 10. There, the applied deformations are large and the solid polymer particulates undergo plastic deformations, which cause large temperature increases in the deforming assembly. The following example serves as a simple illustration of the DEM cycling through a force-displacement constitutive response, $F = k \Delta n$, and Newton's second law, which relates the force to acceleration and, thus, particle motion.

Example 4.2   Soft-Sphere Model DEM Treatment of Two Disks Deformed by Two Rigid Walls   To demonstrate the basic and simple physical model used in DEM, we turn to a pair of two disks, X and Y, compressed between two rigid walls, as shown in Fig. E4.2.

Initially, at $t = t_0$, the walls and disks touch with no force, $F_N = 0$, Fig. E4.2(a). The walls move toward each other at a constant velocity, v. At time $t = t_0 + \Delta t$ the walls have each moved a distance $v\Delta t$. Since the disturbance cannot travel beyond a single disk as assumed by the model, both disks maintain their initial positions during this time interval. Thus, *overlaps* are created at points A and C, Fig. 4.2(b), given by

$$\Delta n = v\Delta t \tag{E4.2-1}$$

The contact A at time $t + \Delta t$ is defined as the halfway point between A_D and A_w. The relative displacement at A is related to the force resulting from the assumed *linear constitutive response* of the particle (that of a simple "spring" in LVE terms)

$$\Delta F_n = k_n (\Delta n)_{t_1} \tag{E4.2-2}$$

At the two disks at $t_1 = t_0 + \Delta t$

$$F_{X_1} = K_n (\Delta n)_{t_1} \qquad F_{Y_1} = -K_n (\Delta n)_{t_1} \tag{E4.2-3}$$

Using Newton's second law of motion to find the accelerations (constant over Δt) of disks X and Y

$$\ddot{X}_1 = \frac{F_{X_1}}{m_X} \qquad \ddot{Y} = \frac{F_{Y_1}}{m_Y} \tag{E4.2-4}$$

By integrating $\dot{X}_1$ and $\ddot{Y}_1$ over t_1 to $t_2 = t_0 + 2\Delta t$, the velocities of the two disks at t_2 are determined by

$$(\dot{X}_1)_{t_2} = \left(\frac{F_{X_1}}{m_x} \right) \Delta t \qquad (\dot{Y}_1)_{t_2} = \left(\frac{F_{Y_1}}{m_y} \right) \Delta t \tag{E4.2-5}$$
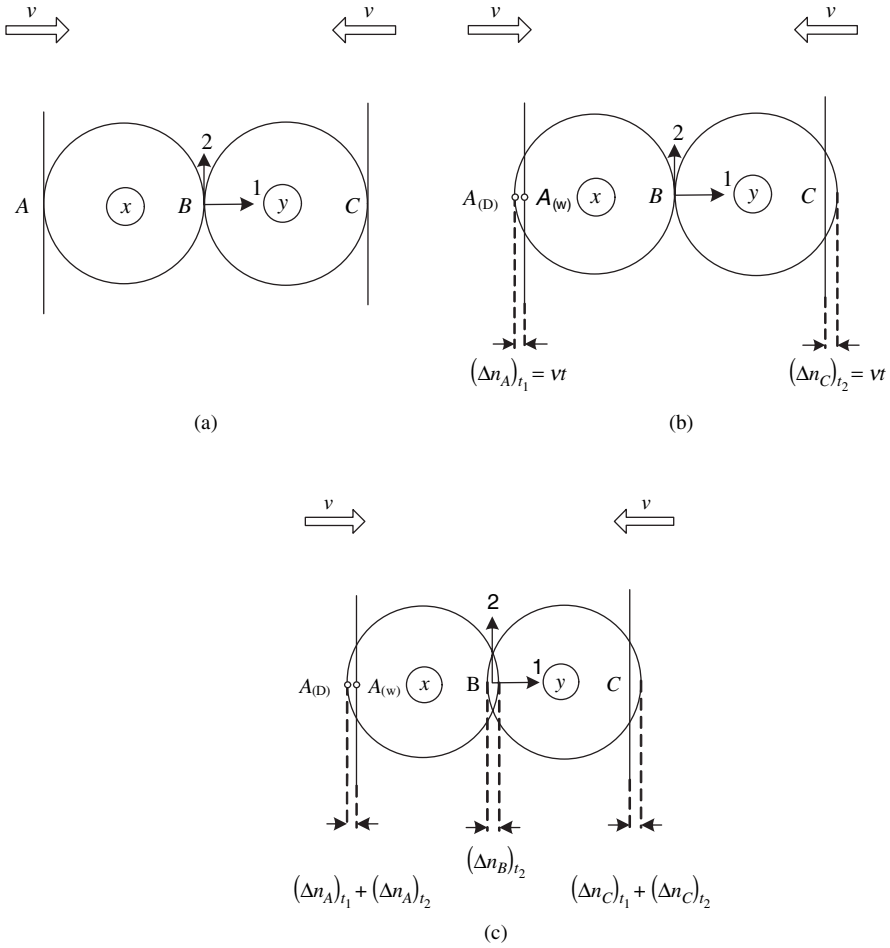
Fig. E4.2 Soft-sphere DEM model for two disks being compressed by two confining walls moving in opposite direction with a velocity v. [Reprinted by permission from P. A. Cundall and O. D. L. Strack, "A Distinct Element Model for Granular Assemblies," *Géotechnique*, **29**, 47–65 (1979).]

Thus the relative displacement at points A, B, and C at t_2 are given by, see Fig. E4.2(a)

$$(\Delta n_A)_{t_2} = \left[v - \left(\frac{F_{X_1}}{m_x} \right) \Delta t \right] \Delta t \qquad \text{(E4.2-6)}$$

$$(\Delta n_B)_{t_2} = \left[\left(\frac{F_{X_1}}{m_X} \right) \Delta t - \left(\frac{F_{Y_1}}{m_Y} \right) \Delta t \right] \Delta t \qquad \text{(E4.2-7)}$$

$$(\Delta n_C)_{t_2} = \left[\left(\frac{F_{Y_1}}{m_Y} \right) \Delta t - (-v) \right] \Delta t \qquad \text{(E4.2-8)}$$

where Δn_i are taken to be positive for compression. This cycle of calculation will be repeated again and again.

In the general case of an assembly with a very large number of disks the calculation cycle is as follows: the $F_i = k \Delta n_i$ is applied at each contact point of any disk and the vectorial sum of the contact forces is calculated to yield the net force acting on the disk. However, for an
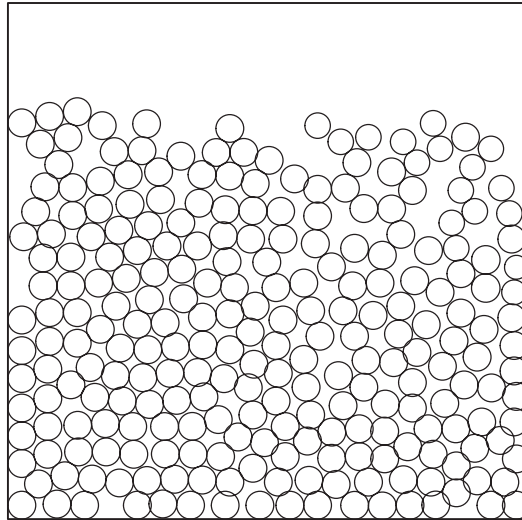
Fig. 4.20 DEM-simulated packing density under gravity for a two-dimensional spherical particulate assembly 50 μm in diameter, with $f' = f'_W = 0.364$ and with van der Waals forces, showing the formation of clusters, which decrease the packing density by more than 10%. [Reprinted by permission from Y. F. Cheng, S. J. Guo, and H. Y. Li, "DEM Simulation of Random Packing of Spherical Particles," *Powder Technol.*, **107**, 123–130 (2000).]

assembly of particles there are both normal and tangential forces, the latter giving rise to moments M_{X_i} and angular acceleration $\ddot{\theta}_{X_i}$, where

$$I_{X_i}\ddot{\theta}_{X_i} = \sum M_{X_i} \tag{E4.2-9}$$

I_{X_i} are the moments of inertia of disks X_i. Interparticle frictional forces are included for both compacted and flowing particulate assemblies

In 1979, Cundall and Strack (41) used the DEM simulation just outlined to compare it with the experiment of de Josselin de Jong (40), and their results are shown in Fig. 4. 17(b). The agreement is excellent, qualitatively, and good, quantitatively. What is important is the fact that this experimental verification of the power of soft-sphere DEM simulations established the field and contributed to its rapid growth.

The soft-sphere DEM is also used to model particulate packing under gravity (50), shown in Fig. 4.20, and particulate flows and fluidization (51,52). DEM simulations scarcely have been used to simulate the pellet/powder behavior under flow or compaction. A notable example is the work of Yung, Xu, and Lau (53) in simulating the conveying of polymer pellets in the solids-conveying region of SSEs. The simulated dependence of the conveying rate on the screw speed, barrel, and screw wall friction coefficients is consistent with that observed experimentally.

REFERENCES

1. H. Rumpf, *Particle Technology*, Dordrecht, The Netherlands, Kluwer, 1990.
2. J. P. K. Seville, U. Tüzün, and R. Clift, *Processing of Particulate Solids*, Dordrecht, The Netherland, Kluwer, 1997.

3. C. Orr, Jr., *Particulate Technology*, Macmillan, New York, 1966.

4. R. L. Brown and J. C. Richards, *Principles of Powder Mechanics*, Pergamon Press, Oxford, 1966.

5. K. Weinghart, "Experiments in Granular Flow," *Annu. Rev. Fluid Mech.*, **7**, 89–114 (1975).

6. D. Dowson, *History of Tribology*, Longman, New York, 1979.

7. R. B. Bowden and D. Tabor, *Friction and Lubrication of Solids*, Oxford Univ. Press, London, 1950.

8. G. Binning, H. Rohrer, Ch. Gerber and E. Weibel, "Surface Studies by Scanning Tunneling Microscopy," *Phys. Rev. Lett.*, **49**, 57–61 (1982).

9. G. Binning, C. F. Quate and Ch. Gerber, "Atomic Force Microscope," *Phys. Rev. Lett.*, **56**, 930–933 (1986).

10. F. Heslot, T. Baumberger, B. Caroli, and C Caroli, "Creep, Stick-slip and Dry Friction Dynamics: Experiments and a Heuristic Model," *Phys. Rev.*, **E49**, 4973 (1994).

11. A. Tanguy, M. Gounelle and S. Roux, "From Individual to Collective Pinning: Effect of Long-range Elastic Interactions," *Phys. Rev.*, **E58**, 1577 (1998).

12. A. S. Lodge and H. G. Howell, *Proc. Phys. Soc. B Band*, **67**, (1954).

13. K. Schneider, *Kunststoffe*, **59**, 97–102 (1969).

14. B. J. Briskoe, C. M. Pooley, and D. Tabor, in *Advances in Polymer Friction and Wear*, Vol. 5A, L. H. Lee, Eds., Plenum Press, New York, 1975.

15. G. H. Qian, I. Bagyi, I. W. Burdick, R. Pfeffer, H. Shaw, and J. Stevens "Gas-Solid Fluidization in a Centrifugal Field," *AIChE J.*, **47**, 1022–1034 (2001).

16. I. Manas-Zlocwover, A. Nir, and Z. Tadmor, *Rubber Chem.Technol.*, **55**, 1250 (1982).

17. K. Allemaskin, I. Manas-Zloczower, and M. Kaufman, "Simultaneous Characterization of Dispersive and Distributive Mixing in a SSE," *Conference Proc., SPE ANTEC*, **61**, 268–272 (2003).

18. H. A. Janssen, "Tests on Grain Pressure Silos," *Z. Vereinsch. Dtsch. Ing.*, **39**, 1045–1049 (1895).

19. Z. Tadmor and C. G. Gogos, *Principles of Polymer Processing*, Section 8.6, Wiley, New York, 1979, Chapter 8.

20. M. Walker "An Approximate Theory for Pressure and Arching in Hoppers," *Chem. Eng. Sci.*, **21**, 975–997 (1966).

21. J. R. Johanson, "Feeding," *Chem. Eng.*, 75–82, (October, 1969).

22. A. W. Jenike, *Gravity Flow of Bulk Solids*, Bulletin #108, Utah Engineering Experimental Station, University of Utah, Salt Lake City, 1961.

23. O. Richmond and G. C. Gardner "Limiting Spans of Arching of Bulk Material in Vertical Channels," *Chem. Eng. Sci.*, **17**, 1071–1078 (1962).

24. J. Lee, S. C. Cowin, and J. S. Templeton "An Experimental Study of the Kinematics of Flow Through Hoppers," *Trans. Soc. Rheol.*, **18**, 247–269 (1974).

25. R. Butterfield, R. M. Harkness, and K. Z. Andrews, "Stereophotogrammetric Methods for Measuring Displacement Fields," *Goetechnique*, **8**, 308 (1970).

26. M. Levinson, B. Smutter, and W. Resnick, "Displacement Velocity Fields in Hoppers," *Powder Technol.*, **16**, 29–43 (1977).

27. M. Nakagawa, S. A. Altobelli, A. Caprihan, E. Fukushima, and E. K. Jeong, "Non-invasive Measurements of Granular Flows by MRI," *Exp. Fluids*, **16**, 54–60 (1993).

28. T. T. Ng, C. Wang, and S. A. Altobelli, "3-D MRI Experiments in Granular Materials," in *Mechanics of Deformation and Flow of Particulate Materials*, C. S. Chang, A. Misra, R. Y. Liang and M. Babic, Eds., ASCE Publication, New York, 1997.

29. H. Potente and T. C. Pohl, "Polymer Pellet Flow out of the Hopper into the First Section of a Single Screw," *Int. Polym. Proc.*, **17**, 11–29 (2002).

30. W. H. Wollaston, *Philos. Trans.*, **119**, 1 (1829).

31. D. Train, "Transmission of Forces Through a Powder Mass During the Process of Pelletizing," *Trans. Inst. Chem. Eng.*, **35**, 262–265 (1957).

32. R. D. Spencer, G. D. Gilmore and R. M. Wiley, "Behavior of Granulated Polymers under Pressure," *J. Appl. Phys.*, **21**, 527–531 (1950).

33. M. Long, "Radial Pressure in Powder Compaction," *Powder Met.*, **6**, 73–86 (1960).

34. H. G. B. Allersma, "Optical Measurements of Stress and Strain in Granular Materials", *Pro. 2nd Int. Conf. Composite Engineering*, New Orleans, LA August 1995, p. 117.

35. C. S. Chang, A. Misra, R. Y. Liang and M. Babic, Eds., *Mechanics of Deformation and Flow of Particulate Materials*, ASCE Publication, New York, 1997.

36. K. Schneider, "Druckausberaitung und Druckverteilung in Schuttgutern," *Chem. Ing. Technol.*, **49** (1969).

37. E. Goldacker, "Untersuchungen zur inneren Reibung von Pulvern, insbesondere im Hinblick auf die Förderung von Extrudern," Dissertation RWTH, Aachen, Germany, 1971.

38. C. Y. Cheng and C. G. Gogos, "Compressibility of Polymer Pellets and Powders," *SPE ANTEC Tech. Papers*, **25**, 156 (1979).

39. K. S. Hyun and M. A. Spalding, "Bulk Density of Solid Polymer Resins as a Function of Temperature and Pressure," *Polym. Eng. Sci.*, **30**, 571 (1990).

40. A. G. de Josselin de Jong and A. Verrijt, *Cah. Grpe fr. Etud. Rheol.*, **2**, 73–86 (1971).

41. P. A. Cundall and O. D. L. Strack, "A Distinct Element Model for Granular Assemblies," *Géotechnique*, **29**, 47–65 (1979).

42. H. G. B. Allersma "Optical Analysis of Stress and Strain in Photoelastic Particle Assemblies," Ph.D. Thesis, Delft University of Technology, Delft, The Netherlands (1987).

43. H. G. B. Allersma "Optical Analysis of Methods to Influence the Stress Distribution in Hoppers" in *Mechanics of Deformation and Flow of Particulate Materials*, C. S. Chang et al., Eds., ASCE Publication, New. York, 1997.

44. S. A. Altobelli, R. C. Gilver, and E. Fukushima, "Velocity and Concentration Measurements of Suspensions by MRI," *J. Rheol.*, **35**, 721–734 (1991).

45. T. T. Ng, M. Kelley, and J. Sampson, *Proc. 11th Engineering Mechanics Conf.*, **1**, 572 (1996).

46. P. A Cundall "A Computer Program for Simulating Progressive Large-scale Movements in Blocky Rock Systems," *Proc. Symp. Int. Soc. Rock. Mech.*, **2**, Nancy, France (1971).

47. D. J. Quensel, D. S. Rimai, and L. P. Demejo, "Molecular Dynamic Modeling of Interfacial Energy," *J. Adhesion Sci. Technol.*, **9**, 1015–1030 (1995).

48. L. Vanel, A. D. Rosato, and R. N. Dave, *Phys. Rev. Lett.*, **17**, 1255 (1997).

49. P. K. Haff, "A Physical Picture of Kinetic Granular Fluids," *J. Rheol.*, **30**, 931–948 (1986).

50. Y. F. Cheng, S. J. Guo, and H. Y. Li, "DEM Simulation of Random Packing of Spherical Particles," *Powder Technol.*, **107**, 123–130 (2000).

51. C. R. Wassgren, C. E. Brennen, and M. L. Hunt, "Vertical Vibration of a Deep Bed of Granular Material in a Container," *J. Appl. Mech.*, **63**, 712–719 (1996).

52. Y. Tsuji, T. Kawaguchi, and T. Tanaka, "Discreet Particle Simulation of Two-dimensional Fluidized Beds," *Powder Tech.*, **77**, 79–87 (1993).

53. K. L. Yung, Y. Xu, and K. H. Lau, "A New Method of Simulating the Conveying of Solid Pellets," *Int. Polym. Proc.*, **17**, 91–94 (2002).

PROBLEMS

4.1. *Friction Between Two Surfaces* Answer the following questions or discuss statements: (a) Two clean, highly polished steel surfaces when brought into contact appear to stick as if having very high coefficient of friction. (b) Would the dynamic coefficient of friction between steel and a polymer increase or decrease with increasing surface

roughness. (c) Why would the dynamic coefficient of friction between polymer pellets and a metal increase with time of rubbing one against the other? How would this affect start-up of solid pellet-fed machines? (d) Would you expect the dynamic coefficient of friction to increase or decrease with metal surface temperature? (e) The dynamic coefficient of friction on a clean surface of LDPE is 0.3 and that of HDPE is 0.08. How do you explain the difference?

4.2. *Effect of Liquids on Friction*   (a) Why do cars tend to slip on a wet road? Why is the risk higher with a worn-out tire? (b) Why do certain people lifting something heavy without gloves spit on their palms? (c) Describe in a short essay how it would be to live in a frictionless world.

4.3. *Solids Height in an Extruder Hopper*   An LDPE-fed SSE is equipped with a 10-cm cylindrical hopper. The operation is sensitive to the pressure under the hopper. If the static coefficient of friction is 0.5 and the ratio of compressive stress in the horizontal direction to compressive stress in the vertical direction is 0.5, what should the minimum height of the solids be in the hopper to secure steady operation?

4.4. *The Effect of Drag on the Pressure Distribution in Solids Filling a Rectangular Channel*   A bed of particulate solids is compressed in a rectangular channel between two freely moving rams, with the upper plate of the rectangular channel moving at a constant velocity. The width of the channel is 5 cm and its height is 0.5 cm. The coefficient of friction on the stationary channel walls is 0.5 and the ratio of axial to perpendicular stresses is 0.4 and can be assumed constant throughout the bed. The force on the downstream ram is 1000 N. (a) Calculate the force that has to be applied on the upstream ram at equilibrium conditions as a function of the coefficient of friction on the moving wall that can be varied in the range of 0 to 1.0. (b) What effect will the doubling of the velocity of the moving plate have on the results in part (a)?

4.5. *Two-dimensional Pressure Distribution in Solids Filling a Rectangular Channel*   Consider the rectangular channel geometry shown in Fig. 4.15. Equation 4.9-7 gives the pressure distribution, accounting for the cross-channel force, but neglecting cross-channel pressure distribution. (a) Show that the down-channel pressure distribution that accounts for cross-channel pressure distribution is given by:

$$\ln \frac{\bar{P}(x)}{\bar{P}(0)} = (R_1 - R_2)x \qquad \text{(P4.6-1)}$$

where $\bar{P}(x)$ is the mean pressure over the cross-section at location x, the same as before

$$\bar{P}(x) = \frac{P(x,0)(e^{R_1 W} - 1)}{R_1 W}$$

where $P(x,0)$ is the axial pressure at $z = 0$ (see Fig. 4.15) and

$$R_1 = f_{w1} \frac{\sin(\theta + \phi)}{H}$$

and

$$R_2 = \frac{f_{w1}\cos(\theta + \phi) - f_{w2}}{H}$$

$$R_3 = \frac{f_{w3}R_1(e^{R_1 W} + 1)}{e^{R_1 W} - 1}$$

where f_{w1}, f_{w2}, and f_{w3} are the coefficients of friction on the moving plate, channel bottom, and channel sidewalls, respectively. (b) Show that for $R_1 W \to 0$, Eq. P4.6-1 reduces to Eq. 4.9-7 with $K = 1$.

4.6. *Flow Rate in a Rectangular Channel*   The pressure profile for drag-induced solids conveying in a rectangular channel is given by Eq. 4.9-7. The channel dimensions are $W = 2.5$ in and $H = 0.5$ in. The pressure at a certain upstream position is 10 psig, and 10 in downstream it is 55.7 psig. The coefficient of friction on the moving wall is 0.5 and 0.2 on the stationary walls. The upper wall moves at an angle of $15°$ to the down-channel direction and at a velocity of 10 in/s. The bulk density is 30 lb/ft^3 and $K = 0.5$. Calculate the mass flow rate of solids.

4.7. *Experimental Determination of the Storage Friction Coefficient, $4Kf_w'$*   Hyun and Spalding[4] developed a polymer particulate solids compaction cell shown schematically in Fig. P4.7(a) and used it to obtain temperature and pressure-dependent bulk density data, as shown on Fig. P4.7(b$_1$) and p4.7(b$_2$).

(a) Comment on the compressibility behavior of the semicrystaline LDPE and amorphous high impact polystyrene (HIPS) (b) the cell was also used to calculate (estimate) the storage friction coefficient $f_s' = 4f_w'K$ in the force balance Eq. 4.5-1. Measuring the top and bottom plunger pressure, they reported the following:

f_s' Values	25°C	50°C	75°C	90°C
LDPE	0.28	0.20	0.18	
HIPS	0.29	0.25	0.24	0.60

Assuming that $P_{avg} = P = (P_{top} + P_{bot})/2$ calculate the ratio of P_{top}/P_{bot} for each temperature. Comment on the physical significance of the results. The inner diameter of the cell is $D = 1.4$ cm and H is height of the bulk material in the cell, $D/H = 0.5$.

4.8. *Calculation of the Particulate Solids Conveying a Screw Feeder*   The performance of a feed screw of 1.0-in flight diameter, 0.325-in screw root diameter and 1.2-in lead was experimentally executed for LDPE pellets with a bulk density of 0.45 g/cm^3 by measuring the mass flow rate in the rotational speed range of 10–215 rpm. The results are shown in the table below. Construct a particulates drag-flow model that calculates with results that are in close agreement with the experimental results.

---

4. K. S. Hyun and M. A. Spalding, *Polym. Eng. Sci.*, **30**, 571 (1990).

Screw Speed (rpm)	Throughput (Exp.) (kg/hr)
10	2.94
20	5.88
50	14.04
100	26.4
150	40.44
200	52.2
215	58.08

4.9. ***The Discreet-Element Method for an Assembly of Two-dimensional Disks***   Example 4.2 serves as a simple illustration of the DEM *cycling* through a *force-displacement constitutive response*, $F_i = k\Delta n_i$ and the *law of motion*, which relates the F_i with $\ddot{X}_i$ and, thus, particle motions. In the general case of an *assembly* with a very large number of disks the calculation cycle is as follows: the $F_i = k\Delta n_i$ is applied at each contact point of any disk and the vectorial sum of the contact forces is calculated to yield the net force acting on the disk. For such an assembly there are both normal and tangential
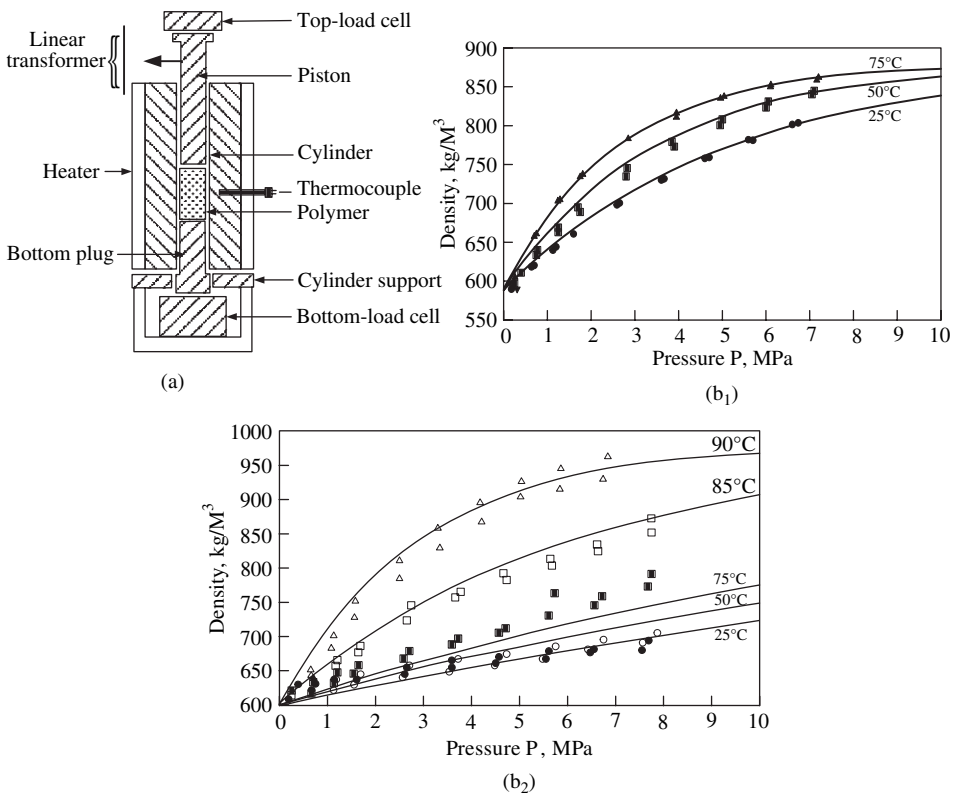

Fig. P4.7   (a) Schematic representation of the compaction cell used by Hyun and Spalding. (b) Experimentally obtained bulk densities of (b_2) LDPE pellets (b_2) HIPS pellets.
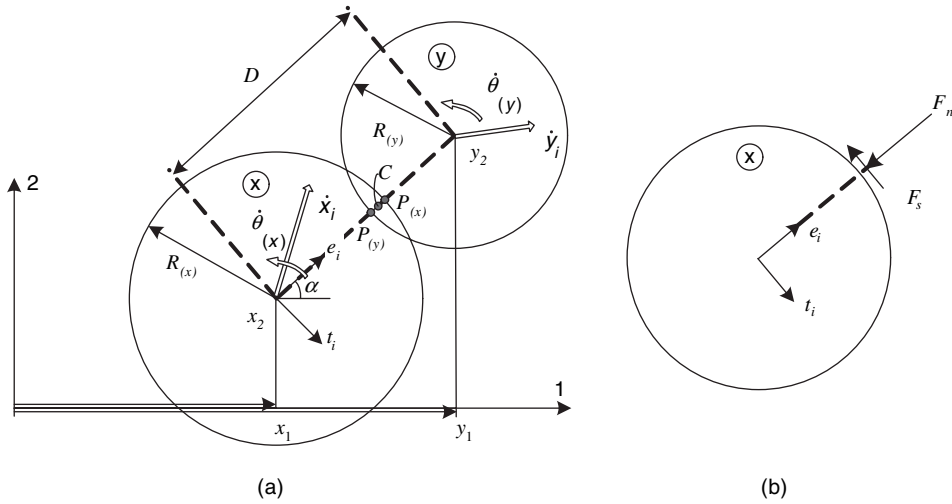
Fig. P4.9   The soft-sphere DEM method for a two-dimenstional assembly, demonstrated by the interaction of two disks, x and y. Positive F_n and F_s are as shown.

forces, the latter giving rise to moments M_{X_i} and angular acceleration $\ddot{\theta}_{X_i}$, where

$$I_{X_i}\ddot{\theta}_{X_i} = \sum M_{X_i}$$

where I_{X_i} are the moments of inertia of disks X_i. After the net forces and moments are determined on every disk of the assembly, new accelerations are calculated for Newton's second law for each disk and, form those, their motions.

   The more general force-displacement two-dimensional DEM method is shown in Fig. P4.9 for a pair of disks x and y in a dynamic state.

   The points $P_{(x)}$ and $P_{(y)}$ are defined as the points of intersection of the line connecting the disk centers with the boundaries of the two disks. Contact takes place if and only if the center-to-center distance D is smaller than the sum of the two disk radii. If this condition is met, the relative (virtual) displacement at the contact C is determined by the integration of the relative velocity, defined as the velocity of point $P_{(x)}$ with respect to $P_{(y)}$. The unit vector $e_i = (\cos\alpha, \sin\alpha) = (y_i - x_i)/D$. The unit vector t_i is obtained by a clockwise $90°$ rotation of e_i, that is, $t_i = (e_2 - e_1)$. The relative velocity of the point $P_{(x)}$ with respect to $P_{(y)}$ can be expressed as $\dot{X}_i$

$$\dot{X}_i = (\dot{x}_i - \dot{y}_i) - (\dot{\theta}_{(x)}R_{(x)} + \dot{\theta}_{(y)}R_{(y)})t_i$$

Calculate (a) the relative normal ($\dot{n}$) and tangential ($\dot{\theta}$) relative velocities and, by integrating the normal and tangential displacements, (b) the increment of the normal ΔF_n and tangential forces ΔF_s using the linear laws $\Delta F_n = k_n\Delta n$ and $\Delta F_s = k_s\Delta s$. (c) Once the normal and shear (tangential) forces are specified for each contact point, the sums $\sum(F_n)_{(x)_i}$ are resolved to the components $\sum(F_n)_{(x_1)}$ and $\sum(F_n)_{(x_2)}$, and the resulting moment on disk x is $\sum M_x = \sum F_s R_{(x)}$; the relations sum the effects of all contacts. From the preceding resultant force and moment on

disk x and Newton's second law on disk x

$$m_{(x)}\ddot{X}_i = \sum (F_n)_{(x)_i}$$
$$I_{(\lambda)}\ddot{\theta}(\lambda) = \sum M(x)$$

Calculate the new velocity and updated position and rotation on each disk.

4.10. ***The Effect of High Single Screw Rotational Speeds in Limiting Operational Mass Throughput Rates***   Potente and Pohl[5] point out that as the single screw rotational speed is increased the actual equipment becomes increasingly smaller than that of the drag throughput rate of the metering section. This is shown on Fig. P4.10. (a) Give the physical reasons for this experimental finding. (b) Given the equipment geometric variables at which rpm value will the throughput rate begin to get affected? $D = 50$ mm, $\theta = 17.4°$, $W = \text{Lead} \times \cos\theta_b - e = D\cos\theta_b - 0.1\ W = 4.4$ cm and $H = 0.5$ cm; the polymer is LDPE pellets with $\rho_b = 0.45$ g/cc. (c) Is this limitation of practical significance?
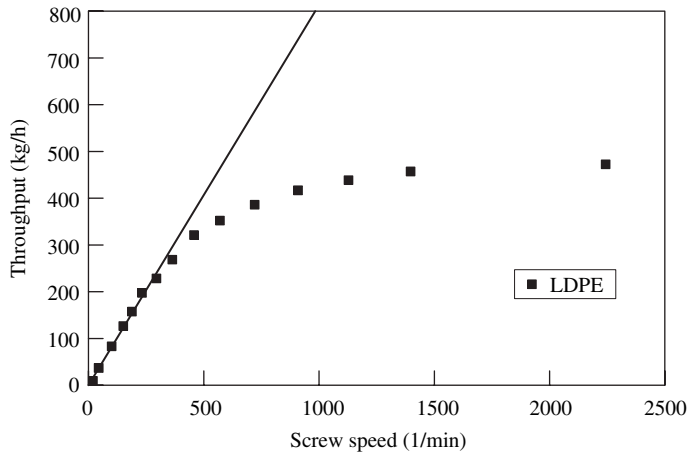

Fig. P4.10   The LDPE throughput rate of a 5 cm square-pitched single screw extruder screw with $e = 0.1\ W$ and $H = 0.5$ cm.

5. H. Potente and T. C. Pohl, *Int. Polym. Process.*, **17**, 11 (2002).